RESEARCH ARTICLE | MARCH 02 2026

Multi-region synergistic discharge with dielectric microstructure in atmospheric oxygen

Junlin Fang ; Bingbing Gu ; Miao Wang ; Shaofeng Xu ; Yongfeng Mei ; Ying Guo ; Jianjun Shi

Phys. Plasmas 33, 033501 (2026)
https://doi.org/10.1063/5.0311816

Physics of Plasmas ARTICLE pubs.aip.org/aip/pop

Multi-region synergistic discharge with dielectric microstructure in atmospheric oxygen

Cite as: Phys. Plasmas **33**, 033501 (2026); doi: 10.1063/5.0311816
Submitted: 12 November 2025 · Accepted: 12 February 2026 ·
Published Online: 2 March 2026

Junlin Fang,[1] Bingbing Gu,[1] Miao Wang,[1] Shaofeng Xu,[1] Yongfeng Mei,[2] Ying Guo,[1,a)] and Jianjun Shi[2,3,a)]

AFFILIATIONS

[1]College of Science, Donghua University, Shanghai 201620, People's Republic of China
[2]Zhejiang Key Laboratory of Extreme Environment Functional Materials, Yiwu Research Institute of Fudan University, Yiwu 322099, People's Republic of China
[3]State Key Laboratory of Surface Physics & International Institute for Intelligent Nanorobots and Nanosystems, College of Intelligent Robotics and Advanced Manufacturing, Fudan University, Shanghai 200438, People's Republic of China

[a)]**Authors to whom correspondence should be addressed:** guoying@dhu.edu.cn and jianjunshi@gmail.com

ABSTRACT

The synergistic discharge in atmospheric oxygen is investigated with a two-dimensional fluid model by introducing periodic micro-slit structures on the dielectric surface, in which the spatiotemporal evolution of the electric field and particle in terms of electrons reveals a discharge enhancement mechanism. The applied longitudinal electric field in the micro-slits governs the ionization wave formation and propagation while enabling the development of a transverse electric field. As the ionization wave propagates into the bulk discharge region, its longitudinal electric field superimposes with the transverse electric field, which significantly enhances the discharge intensity. Meanwhile, the transverse field redistributes electrons, which strengthens the local electric field and the electron energy accordingly. It proposes a synergistic mechanism characterized by the superposition in oxygen discharge of longitudinal and transverse electric fields, offering a new strategy for efficient generation of atomic oxygen.

I. INTRODUCTION

Atmospheric-pressure dielectric barrier discharge (DBD) can generate various reactive species, including reactive gases (such as O_3, NO, and NO_2) and free radicals (such as OH, O, and N).[1–5] It is widely applied in environmental remediation for wastewater purification,[6,7] sterilization, and medical treatments,[8–10] as well as for generating atomic oxygen and ozone in oxygen discharge, which are used in thin film formation processes via CVD and ALD.[11–13] It is well-known that air or oxygen discharge requires a higher reduced electric field and energy consumption. The discharge characteristics of plasma are primarily influenced by both the discharge configuration and the excitation source.

Most oxygen discharge processes are implemented in sub-millimeter-scale parallel-plate or coaxial configurations in order to achieve relatively high oxygen discharge intensity.[14,15] However, under atmospheric-pressure conditions, the ozone concentration remains relatively low; the actual generation efficiency is typically far lower than the theoretical value.[16,17] To address this issue, related studies have focused on modifying the discharge structure to enhance the discharge. For example, it has been reported that employing a strip-shaped powered electrode structure in oxygen discharges can couple the surface discharge on the electrode with the volume discharge in the region between the powered and grounded electrodes, resulting in a significant enhancement compared with a single discharge mode.[18] However, although the grooves formed by the modified powered electrode geometry were shown to intensify the discharge, the underlying physical mechanism responsible for this enhancement has not been further clarified. Related experimental investigations have shown that the presence of microhole structures on or within dielectric tubes can significantly enhance oxygen discharges.[19] Wang *et al.* studied the discharge characteristics of dielectric micropores and found that discharges inside the micropores initiate more rapidly and exhibit higher intensity.[20] In addition, other studies have performed comparative analyses before and after filling dielectric surfaces with SiO_2 or coating them with ZnO, revealing that a large number of microstructures are formed on the dielectric surface after treatment, which markedly

improves oxygen discharge performance.[21,22] Although these experimental results highlight the advantages of microstructure-assisted discharges, the enhancement mechanism associated with microstructure-induced spatial electric-field reconstruction has not yet been explained from the perspective of electron kinetics. Furthermore, it has been reported that ionization waves generated in different regions of the discharge space may interact in a complex manner, and such interactions can further strengthen the overall discharge. Naidis and Babaeva investigated the interaction among three plasma jet tubes and found that, as the spacing between the jets decreased, the coupling and interaction between the jets became progressively stronger.[23] Ghimire *et al.* demonstrated that spatially controlled multi-jet coupling can enhance discharge intensity by up to approximately nine times compared with a single jet.[24] Therefore, experimental and numerical studies involving the introduction of microstructures on dielectric surfaces not only help to elucidate the enhancement mechanisms of multi-region synergistic discharges but also offer new insights and technical pathways for the design of high-efficiency ozone generators, low-power plasma devices, and the processing of micro- and nano-scale functional materials.

The excitation source is also an important factor influencing discharge characteristics. Pulse power sources achieve instantaneous high reduced electric fields by adjusting the rise time (on the nanosecond scale). It enables more efficient energy transfer to electrons, resulting in higher electron energy. It allows for separate control of electron energy and gas temperature, preventing gas overheating while maintaining a high concentration of reactive particles. Regarding pulse and AC excitation sources, studies have pointed out that pulse excitation reduces the electrical energy consumption by 12 times compared to AC while generating the same number of oxygen atoms.[25] In air discharge research, Jiang *et al.* indicated that pulse discharge is more likely to achieve uniform glow discharge compared to AC, enhancing discharge uniformity and efficiency.[26] Meanwhile, Wang *et al.* demonstrated that pulse discharge has lower thermal effects and higher discharge efficiency compared to AC, which is highly advantageous for ozone generation in oxygen discharge, as ozone is prone to thermal decomposition.[27]

Studies on oxygen discharge have revealed that glow discharge exhibits higher efficiency compared to streamer discharge, and its absence of high-temperature discharge channels results in significantly lower heat generation. Furthermore, the efficiency of streamer discharges is largely determined by the effective discharge region.[15] To enhance discharge performance, previous studies have investigated the effect of different electrode materials on discharge characteristics. It has been demonstrated that electrode materials can modulate the energy injected into the electric field, thereby influencing the generation of reactive species.[28,29] Liu *et al.* further showed that silver electrodes can sustain stable glow discharges during the negative half-cycle of AC excitation in oxygen, leading to improved discharge efficiency.[30] In summary, the combination of excitation source control, spatial microstructure design, and efficient catalytic materials offers a promising strategy for achieving high-performance discharge modes.

This study employs a two-dimensional fluid model to investigate the enhancement of pulsed oxygen discharge at atmospheric pressure induced by dielectric surface microstructures. By analyzing the electron dynamics, the generation and evolution of the electric field, as well as the transport and spatial distribution of charged species across multiple regions, the study reveals a spatially synergistic discharge enhancement mechanism, in which microstructures facilitate electric-field superposition and regulate electron motion.

II. DESCRIPTION OF THE MODEL

Periodic slits are constructed on a single dielectric surface as shown in Figs. 1(a) and 1(b). The slit width is denoted as x_1, the depth as y_2–y_1, and the spacing between slits as x_2, where y_1 is 0.15 mm and y_2 is 0.60 mm. In the diagram, region A corresponds to the dielectric surface slit discharge, and region B to the bulk discharge. The pink luminescent regions depict the oxygen discharge plasma. In terms of mesh configuration, the dielectric region has a cell size of 0.01 mm by 0.005 mm (height × width), whereas both the raised microstructure and the plasma region are discretized with a uniform mesh of 0.005 mm.

In the experiment and simulation, the groove width ($x_1 = 2$ mm) and spacing ($x_2 = 2$ mm) are set, and the waveforms of the pulsed discharge voltage and current density are shown in Figs. 1(c) and 1(d). The pulse duration of the applied voltage is 2.0 μs, with rise and fall durations of 50 ns each, and a repetition frequency and amplitude of 7 kHz and 8 kV. The experimental maximum current densities are 0.124×10^4 and 0.122×10^4 A/m^2, corresponding to the discharge events on the rising and falling phases,[31] respectively. The simulated voltage and current waveforms show good agreement with the experimental results, as illustrated in Fig. 1(d).

The microstructural enhancement mechanism will be examined through a detailed analysis of the simulated discharge process using a slit width of 0.1 mm. The pulse discharge voltage and current density waveforms are shown in Fig. 2(a). Its trend in current density is consistent with that in Figs. 1(c) and 1(d). Figure 2(b) presents the total electric-field vector at the ionization wave front, where the white arrows indicate the field direction and their lengths represent the field strength. Once the ionization wave enters the bulk discharge region, the locally enhanced electric field at the wave front radiates across a broad region of the bulk discharge region.

The plasma module in COMSOL Multiphysics self-consistently describes ionization, recombination, excitation, and other reaction processes in the discharge region by solving the transport equations for charged particles together with the electric-field equations. It is an important tool for simulating atmospheric-pressure plasmas. The module is based on the drift-diffusion approximation and the quasi-neutrality assumption, and it can solve for key parameters such as electron density, ionization region distribution, and electron energy under given gas compositions, reaction mechanisms, and applied potential conditions. Previous studies on helium, argon, and oxygen discharges have confirmed, through COMSOL's plasma module,[32–36] their feasibility for generating low-temperature plasmas. The number density of plasma species is obtained by solving the continuity equations

$$\frac{\partial n}{\partial t} + \frac{\partial \Gamma_x}{\partial x} + \frac{\partial \Gamma_y}{\partial y} = S, \tag{1}$$

where n, Γ, and S are the number density, the flux, and the sources of plasma species, respectively. The subscripts x and y correspond to the axial and radial directions, respectively. The fluxes of ions and electrons are as follows:

$$\Gamma_{i,e}(x) = \pm \mu_{i,e} n_{i,e} E_x - D_{i,e} \frac{\partial n_{i,e}}{\partial x}, \tag{2}$$

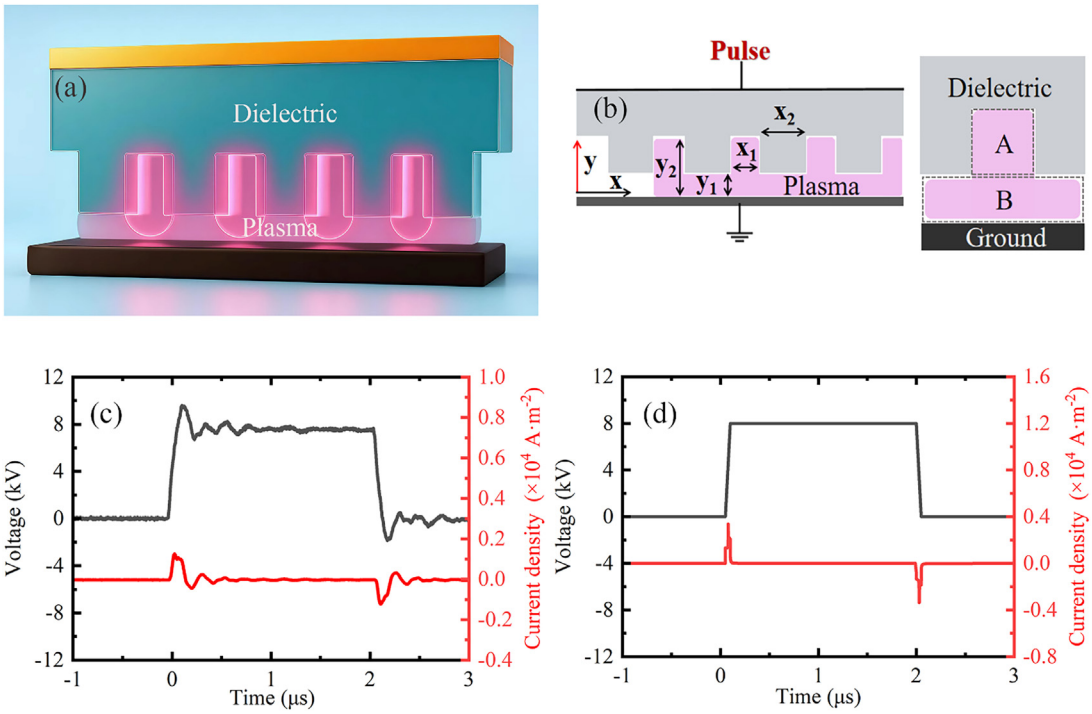

FIG. 1. (a) and (b) Structure of the device. (c) Experimented with measured waveforms of voltage and current density. (d) Simulated waveforms of voltage and current density.

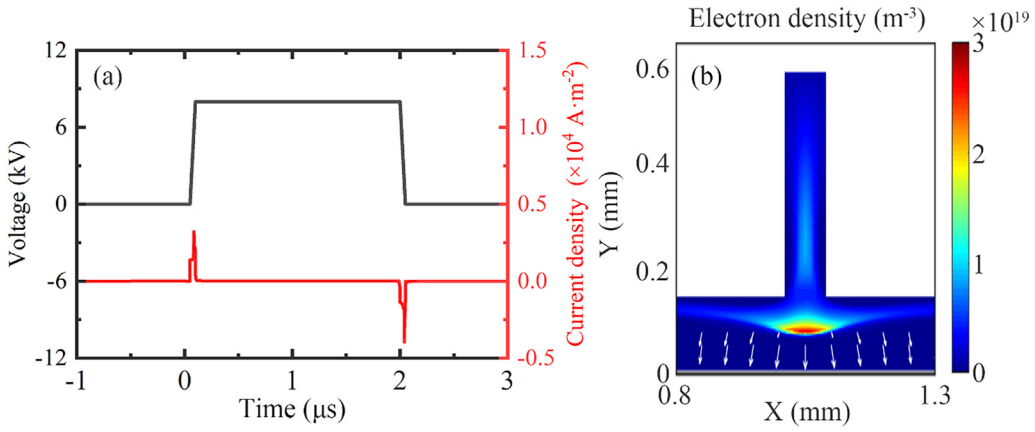

FIG. 2. (a) Simulated waveforms of voltage and current density. (b) Discharge effect diagram.

$$\Gamma_{i,e}(y) = \pm\mu_{i,e}n_{i,e}E_y - D_{i,e}\frac{\partial n_{i,e}}{\partial y}, \tag{3}$$

where i and e denote ion and electron, and μ and D are the coefficients of mobility and diffusivity, respectively. The electrical field E can be obtained by solving the Poisson's equation

$$\varepsilon_r\varepsilon_0\left(\frac{\partial E_x}{\partial x} + \frac{\partial E_y}{\partial y}\right) = e\left(\sum_p n_{i,p} - n_e\right), \tag{4}$$

where ε_0,ε_r and e are the vacuum permittivity and elementary charge, respectively. In this study, the relative permittivity (3) of the dielectric.

Electron mean energy ε can be calculated as follows:

$$\frac{\partial(n_e\varepsilon)}{\partial(x)} = -\frac{\partial\Gamma_\varepsilon}{\partial x} - \varepsilon\Gamma_e E - K_{L,ij}(\varepsilon)n_i n_j - 3\left(m_e/m_{neut}\right)NK_{mt}n_e k(T_e - T_{neut}), \tag{5}$$

where T is the temperature of plasma species, and m is the mass of plasma species. $K_{i,j}$ and $K_{L,ij}$ are the reaction rate and the energy

gain/ loss rate attributed to the reaction between species i and j, respectively. K_{mt} is the momentum transfer frequency corresponding to the elastic collision between electrons and background gas molecules. The relevant reaction equations, model parameters, and model validation can be found in the supplementary material.

The continuity equation for each species requires boundary conditions at both electrodes: the net flux of a particle/species is equated to the difference between loss and creation of that plasma species.

For electrons, secondary electrons emitted from the electrodes through bombardment of ions are considered here, and their loss to the electrodes due to absorption and recombination is not included in this model. Therefore,

$$\Gamma_e = \gamma \sum \Gamma_{ion}, \tag{6}$$

where γ (0.05) is the secondary emission coefficient and is determined by the material and surface conditions of the electrode.

For neutral particles, ions, and metastables, the flux at the electrodes is dominated by drift, and their diffusive flux is negligible. Hence,

$$\partial n/\partial x = 0. \tag{7}$$

A structured rectangular grid set the maximum edge length of each mesh element to 0.01 mm and the minimum to 0.005 mm. It ensures accurate resolution of the steep gradients in the electric field and particle density near the electrode edges and dielectric microstructures, avoiding errors caused by sharp features in specific regions. The total degrees of freedom in the model exceed 1.0×10^6, ensuring high computational accuracy and stability. Additionally, we conducted a mesh independence test, which demonstrated that further mesh refinement resulted in changes of less than 5% in the calculated peak electric field and oxygen atom density, verifying the numerical stability of the model.

Numerous relevant literature has confirmed from experimental and applied perspectives that such microstructures promote discharge.[6,19,37–39] The related reaction equations[40] and corresponding experimental validation work are provided in more detail in the supplementary material.

III. RESULTS AND DISCUSSION

A. Comparison of discharge with and without microstructures

As shown in Figs. 3(a-I) and 3(b-I), when the ionization wave propagates to the same position in the bulk discharge region, the presence of microstructures significantly enhances discharge characteristics. Specifically, the electron density at the ionization wave front is nearly an order of magnitude higher with microstructures compared to the case without them, indicating stronger ionization.

In Fig. 3(a-II), the peak longitudinal electric field without microstructures is 6.86×10^6 V/m. This value is marked by a white dashed line in Fig. 3(b-II), which clearly outlines the expanded region where the electric field exceeds this threshold in the presence of microstructures. Remarkably, the peak Ey further rises to 8.75×10^6 V/m, highlighting the significant field enhancement due to the slit design.

Furthermore, as seen in Fig. 3(b-III), the electron energy within the region enclosed by the white dashed line is higher than the maximum electron energy (7 eV) in the case without

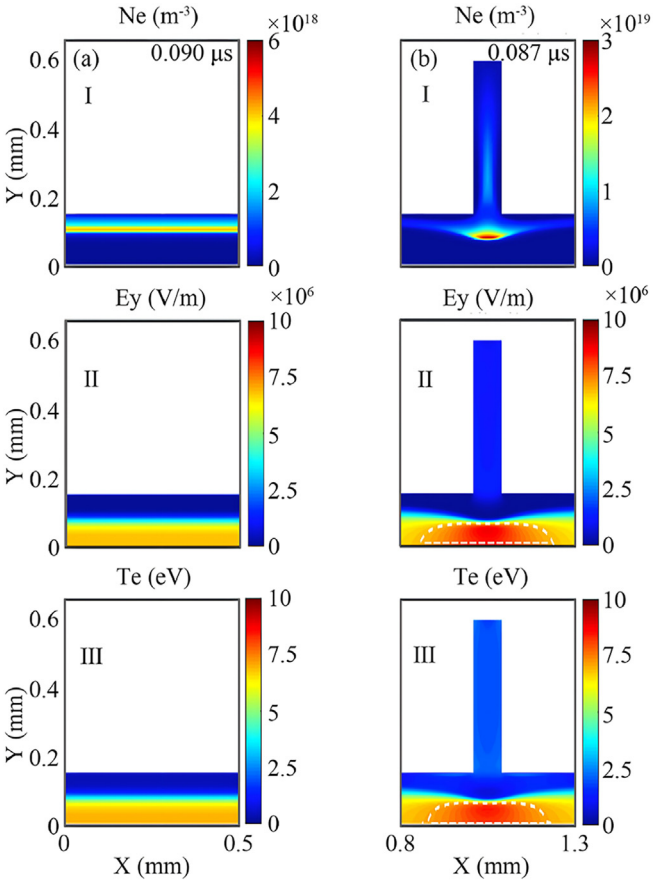

FIG. 3. Comparison of the spatial electron density (*ne*), longitudinal electric field (*Ey*), and electron energy (*Te*) at the same position in the main discharge region without (a-I, II, III) and with (b-I, II, III) microstructures.

microstructures. According to the total electric-field vector distribution at the ionization wave front shown in Fig. 2(b), the locally enhanced electric field covers a relatively wide area within the bulk discharge region. Its longitudinal component aligns with the direction of the applied electric field, resulting in a longitudinal superposition effect. Furthermore, by combining the observations from Figs. 3(b-II) and 3(b-III), it can be seen that the region of significantly enhanced electric field corresponds precisely to the radially distributed range of the locally enhanced field shown in Fig. 2(b). In addition, the region where electron energy is increased (indicated by the white dashed line) closely coincides with the region of enhanced longitudinal electric field. This indicates that electrons are primarily accelerated under the dominant effect of the locally enhanced longitudinal electric field, thereby gaining higher energy.

The discharge without microstructures exhibits typical parallel-plate discharge characteristics, with a uniform ionization wave driven solely by the applied longitudinal electric field. In contrast, the discharge mode with microstructures is a hybrid of jet-like and parallel-plate modes. The ionization wave head, formed within the slit structure, locally enhances the electric field. When the ionization wave

enters the bulk discharge region, the superposition of its longitudinal electric field enhances the overall electric field, leading to an increase in electron energy and an intensification of the discharge.

B. Evolution of multi-region synergistic discharge

As shown in Fig. 4, the evolution of spatial electron density, transverse electric field (*Ex*), and longitudinal electric field (*Ey*) is presented inside the slit.

From Fig. 4(a), it can be seen that the discharge initiates at the powered electrode. Electrons initially accumulate near the dielectric surface, forming a distinct local enrichment region. At this stage, a pronounced electron density gradient develops between the center and the sides of the slit. As time progresses, the ionization wave propagates toward the grounded electrode. The discharge is mainly concentrated in the central region due to the initial electron density distribution, as shown in Fig. 4(a-II). When the ionization wave enters the bulk discharge region, it further enhances ionization in the transverse regions. This process promotes the formation of a larger bulk discharge, as illustrated in Figs. 4(a-III) and 4(a-IV); the electron density is on the same order of magnitude as reported in the relevant literature.[41–44]

Figure 4(b) shows the evolution of *Ex* during ionization wave propagation within the slit. As the ionization front advances, compressed *Ex* regions form on both sides. The peak *Ex* increases from 2.25×10^6 to 3.15×10^6 V/m and then gradually decreases to 2.75×10^6 V/m.

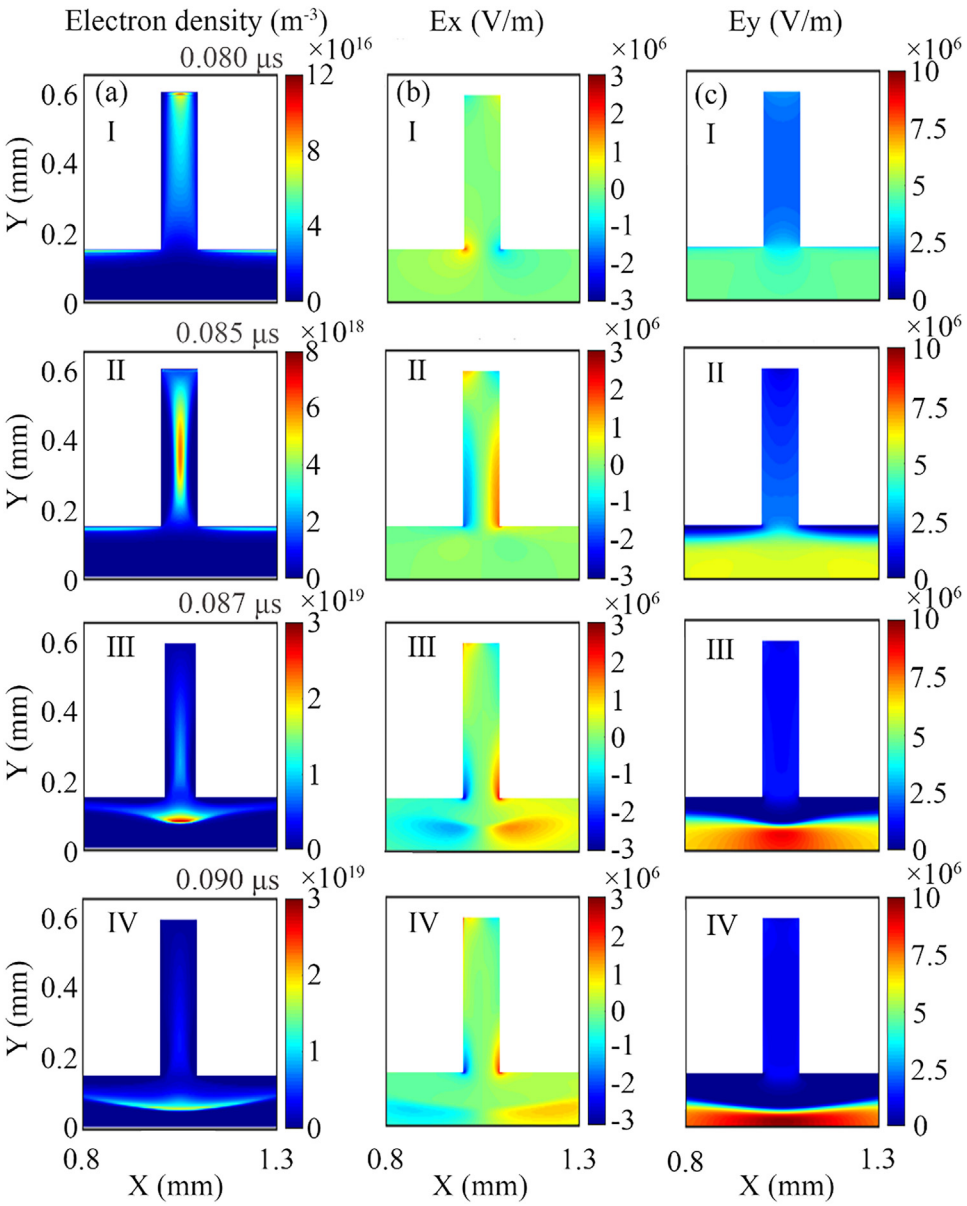

FIG. 4. (a) Evolution of spatial electron distribution in the slit region. (b) Evolution of the *Ex*. (c) Evolution of the *Ey*.

Figure 4(c) illustrates the enhancement of *Ey* at the ionization wave front. The peak *Ey* increases from 4.55×10^6 to 9.61×10^6 V/m. When the ionization wave reaches the bulk discharge region, the longitudinal electric field at the wave head is no longer confined by the slit. It radiates into the larger bulk discharge regions on both sides, leading to a significant enhancement of the electric field. This magnitude is consistent with the typical electric-field intensity observed in strong air discharges under atmospheric pressure and reaches a level comparable to that of needle-point discharge structures,[45–47] which clearly demonstrates the significant advantage of this configuration in electric-field enhancement.

In addition to the analysis of the electric field, examining the charged particle dynamics inside the slit can reveal the formation mechanism of the enhanced electric field within it. Figures 5(a)–5(d) show the spatial distributions of positive and negative particles, as well as the transverse and longitudinal flux distributions of electrons and O_2^+, along Y = 0.25 mm inside the slit at different times. As shown in Fig. 5(a), before the ionization wave reaches the 0.25 mm position (Y), the spatial peak number density of O_2^+ is 0.94×10^{18} m^{-3} and that of negative particles is 0.48×10^{18} m^{-3}. When the ionization wave arrives at this location, as illustrated in Fig. 5(b), the spatial peak number density of O_2^+ increases to 8.08×10^{18} m^{-3}, while that of negative particles rises to 6.30×10^{18} m^{-3}. At this moment, a significant numerical difference exists between the positively and negatively charged particles.

Figure 5(c) shows the total drift-diffusion flux of electrons along Y = 0.25 mm, with dashed lines representing transverse flux and solid lines longitudinal flux; the symbols indicate flux directions. At the initial stage of discharge propagation (t = 0.083 μs), the electron longitudinal flux peaks at 0.064×10^{24} m^{-2} s^{-1}, and the transverse electron flux is much smaller than the longitudinal flux, reaching only on the order of 10^{21}.

Figure 5(d) shows the total drift-diffusion flux of electrons and O_2^+ along Y = 0.25 mm, with dashed lines representing transverse flux and solid lines longitudinal flux; the symbols indicate flux directions. At t = 0.085 μs, the electron longitudinal flux peaks at 0.99×10^{24} m^{-2} s^{-1}, and the transverse flux reaches 0.067×10^{24} m^{-2} s^{-1}. In contrast, the O_2^+ longitudinal and transverse fluxes are only 9.30×10^{21} and 1.98×10^{21} m^{-2} s^{-1}, respectively, showing that electron drift and diffusion rates are approximately two orders of magnitude higher than those of ions.

The formation and evolution of the transverse electric field are mainly induced by the action of the longitudinal electric field. In the initial stage, driven by the externally applied longitudinal electric field, electrons accelerate and drift toward the powered electrode [see Fig. 5(c)], which breaks the local space-charge balance and results in a net positive charge distribution in localized regions [see Fig. 5(a)], thereby giving rise to the initial transverse electric field,[40] according to the charge distribution, the transverse electric field is directed toward both sides. At this stage, the difference in the quantities of positive and negative charges is relatively small. Under the regulation of the transverse electric field, electrons converge from both sides toward the central region, leading to an increase in electron density in the center [see Fig. 5(d)]. According to the collision reaction rate relationship, $k \propto f(T_e,\ n_e)$, an increase in electron density thus enhances the

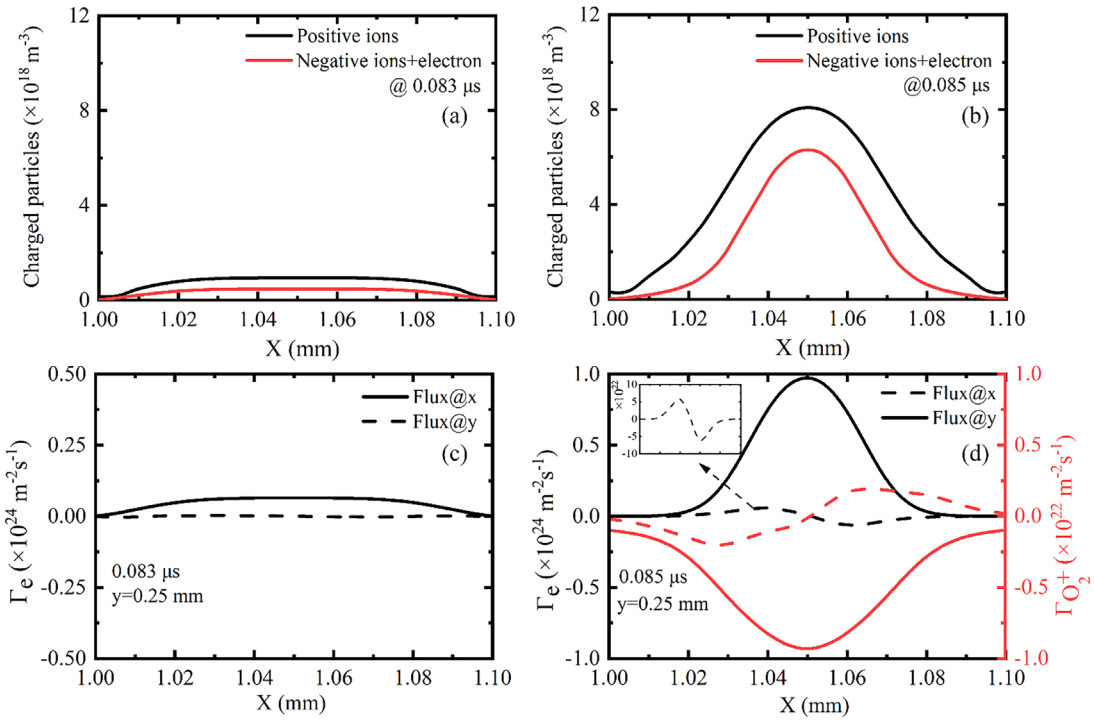

FIG. 5. (a) The spatial distribution of positive and negative particles along Y = 0.25 mm (0.083 μs). (b) The spatial distribution of positive and negative particles along Y = 0.25 mm (0.085 μs). (c) The total transverse and longitudinal flux components of electrons along Y = 0.25 mm (0.083 μs). (d) The total transverse and longitudinal flux components of electrons and O_2^+ (0.085 μs).

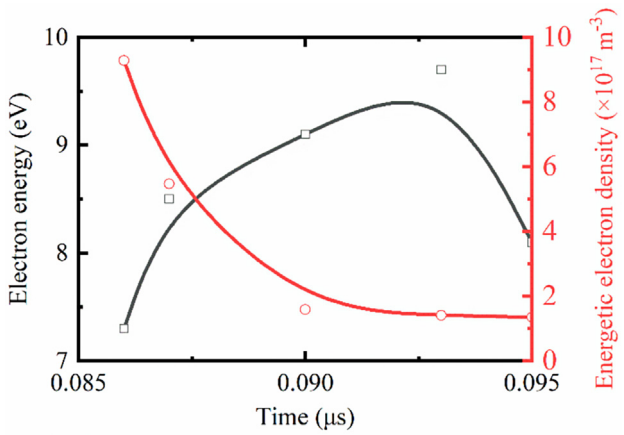

FIG. 6. The peak electron energy at the X = 1.05 mm line and the peak density of energetic electrons in the ionization wave head region.

ionization reactions, generating more charged particles. Under the action of the longitudinal electric field, charged particles undergo further drift, leading to a more pronounced charge separation effect [see Fig. 5(b)]. Meanwhile, the externally applied electric field increases with time, which further strengthens the longitudinal electric field and consequently intensifies charge separation at the head of the ionization wave. The continuous accumulation of positive ions at the wave front promotes a simultaneous enhancement of both the transverse and longitudinal electric fields. The strengthened electric fields, in turn, further drive electron drift and ionization processes in both the transverse and longitudinal directions during subsequent stages. This coupled and self-reinforcing process ultimately forms a positive feedback mechanism for electric-field enhancement.

Figure 6 reflects the temporal evolution of peak electron energy and the peak density of energetic electrons in the ionization wave head region (energy >6 eV). As the ionization wave advances, the electron energy initially increases and then decreases, while the peak density of energetic electrons declines from 9.27×10^{17} to $1.35 \times 10^{17}\ m^{-3}$. As the ionization wave propagates, although the peak electron energy gradually increases, the peak density of energetic electrons exhibits a decreasing trend. This behavior arises because the undischarged region ahead of the ionization wave front progressively shrinks during propagation. Since this region possesses the highest electric field and serves as the primary source of energetic electron generation, the reduction in its spatial extent directly leads to a decrease in the peak density of energetic electrons. The reaction intensity—particularly for the dominant oxygen ionization reaction, $e + O_2 = O_2^+ + 2e$—is jointly governed by both the electron energy and the density of energetic electrons. Therefore, the reduction in the peak density of energetic electrons is identified as the primary factor responsible for the observed weakening of the discharge, as illustrated in Fig. 4(a-IV).

In addition, this study analyzes the evolution of the bulk discharge process corresponding to the dielectric region ($x_2 = 1.1$–2.1 mm). As shown in Fig. 7(a), the bulk discharge region ignites at the central surface region of the dielectric. Subsequently, the electron density in the regions on both sides rises from the order of 10^{16} to $10^{18}\ m^{-3}$, the discharge intensity on both sides gradually surpasses those in the central region as time progresses.

Figure 7(b) shows that at 0.085 μs, when the ionization wave within the slit reaches the slit opening [see Fig. 4(a)], the total transverse electron flux near X = 2.1 mm rapidly surges from a peak value of 1.00×10^{22} to $1.50 \times 10^{23}\ m^{-2}\ s^{-1}$. The drift direction shifted from the center of the bulk discharge region corresponding to the dielectric toward that corresponding to the slit. It indicates that the transverse electric field redistributes the electrons, increasing the electron density in the bulk discharge region near the slit opening. Combined with the radiation effect of the locally enhanced electric field, as shown in Figs. 2 and 4, not only is the transverse electric field enhanced at this stage, but the longitudinal electric field is also synchronously intensified. Superimposed with the externally applied electric field, they collectively strengthen the overall electric field in the bulk discharge region corresponding to the dielectric, with the field magnitude increasing in proximity to the slit. This combined mechanism further promotes the transverse expansion of the discharge region originating from the slit.

C. Mechanism of discharge enhancement by locally enhanced transverse and longitudinal electric fields

As shown in Figs. 8(a) and 8(b), when the ionization wave propagates into the bulk discharge region, the locally enhanced longitudinal electric field continues to radiate outward. This radiation expands its region of influence and increases the peak longitudinal electric field on both sides of the bulk discharge region. At the same time, the electron energy rises significantly. Its evolution trend is closely aligned with that of the longitudinal electric field. These results indicate that the longitudinal electric field not only governs ionization wave propagation but also plays a key role in accelerating electron energy acquisition.

Figures 8(c) and 8(d) further show that a transverse electric field is consistently present at the ionization wave front during propagation. This field acts on almost the entire bulk discharge region. Under its influence, electrons continuously drift from both sides toward the ionization wave front. This drift enhances the local charge density and ionization rate. As a result, a high discharge intensity is sustained at the wave front. This transverse electron transport mechanism strengthens the continuous propagation of the ionization wave.

As indicated by the electric-field evolution in Fig. 8, when the ionization wave enters the bulk discharge region, the transverse electric field does not continue to increase monotonically, reflecting the convergent nature of the positive feedback enhancement between the transverse and longitudinal electric fields discussed above. After the slit ionization wave enters the bulk discharge region, the longitudinal electric field continues to strengthen before reaching the grounded electrode (prior to 0.095 μs). In contrast, the transverse electric field exhibits an initial increase followed by a decrease. As shown in Fig. 7, the initial enhancement arises from transverse electron migration, which leads to a local increase in electron density, thereby intensifying the discharge and charge separation and temporarily strengthening both the transverse and longitudinal electric fields. Subsequently, the transverse electric field begins to weaken. As can be seen from Fig. 4, this weakening trend is essentially consistent with the decay of the discharge intensity, indicating that the discharge attenuation reduces charge difference within the bulk discharge region. The primary reason for the discharge weakening is the decrease in the density of energetic electrons within the discharge space as the ionization wave propagates, as shown in Fig. 6. In addition, oppositely directed transverse electric

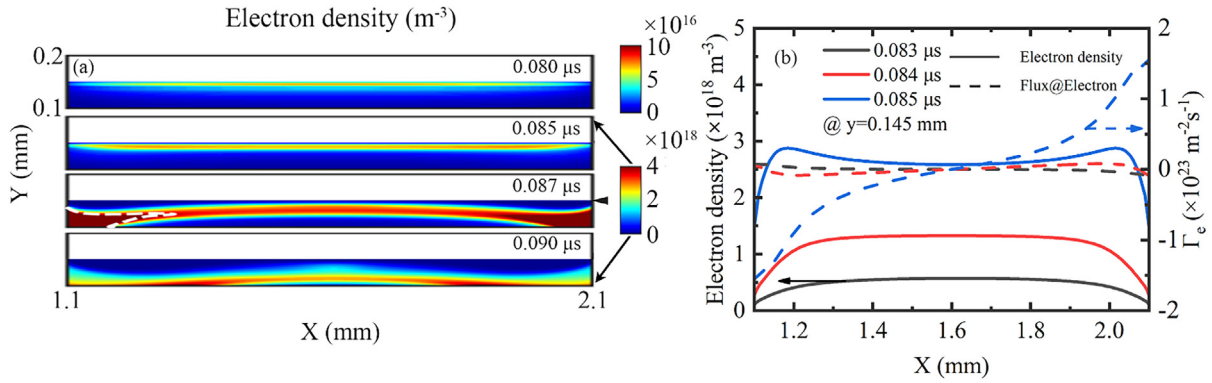

FIG. 7. (a) Temporal evolution of the bulk discharge region corresponding to the dielectric. (b) Electron density distribution and total transverse flux on the dielectric surface.

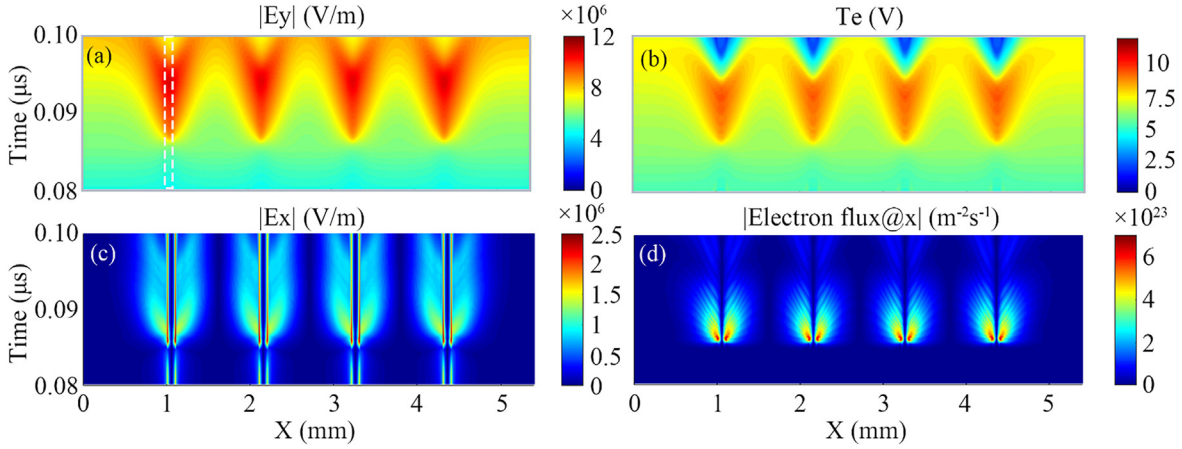

FIG. 8. Time evolution of peak values (compressed along Y) in the bulk discharge region after the ionization wave reaches it: (a) *Ey*. (b) Electron energy. (c) *Ex*. (d) Transverse electron flux. The white dashed-line region represents the temporal evolution of the bulk discharge region corresponding to the slit.

fields generated by adjacent micro-slits in the same region can partially cancel each other, as illustrated in Fig. 8(c), further weakening the electric field. The reason why the longitudinal electric field can continue to increase is that the potential drop is mainly concentrated between the ionization wave head and the grounded electrode. These factors collectively account for the inherent limitations in the enhancement of the transverse and longitudinal electric fields.

D. Results of the enhancement of the bulk discharge

To further clarify the impact range of the slit-enhanced discharge in the bulk region, Fig. 9(a) shows the distributions of the peak longitudinal electric field, electron energy, and electron reaction rate along $Y = 0.05$ mm at various X positions. In the figure, the overall reaction intensity is represented by the reaction rate of the dominant electron-impact processes ($e + O_2 = O_2^+ + 2e$). The variation trend of this rate is consistent with the generation rate of oxygen atoms ($e + O_2 = 2O + e$), indicating the spatial distribution of oxygen atom production. Since ozone formation primarily depends on the concentration of oxygen atoms ($O + O_2 + O_2 = O_3 + O_2$),[18,48] the regions of efficient ozone generation can thus be identified. From both sides toward the center of the slit-corresponding bulk discharge region, the electron-impact reaction rate constant k_e increases from 0.39×10^4 to 2.90×10^4 mol m^{-3} s^{-1}. This trend is consistent with the enhanced electric field, elevated electron energy, and strengthened transverse electron transport observed in the bulk discharge region in Fig. 8. Taken together, these results indicate that the transverse electric field drives electrons to converge toward the slit center. This process leads to an increase in the local electron density. In contrast, the longitudinal electric field mainly governs the enhancement of electron energy. The combined action of these two electric-field components significantly intensifies collisional ionization reactions. This interaction forms a positive feedback loop among the electric field, electron transport, and reaction enhancement. As a result, the discharge undergoes transverse expansion and can be sustained more effectively. The blue dashed line indicates the maximum reaction rate without microstructures, while the blue rectangle denotes the projection of the slit onto the bulk discharge region. Within the slit projection region, all three parameters are significantly enhanced and gradually decay in the transverse direction. Notably, at approximately $x = 1.6$ mm, the reaction rate falls

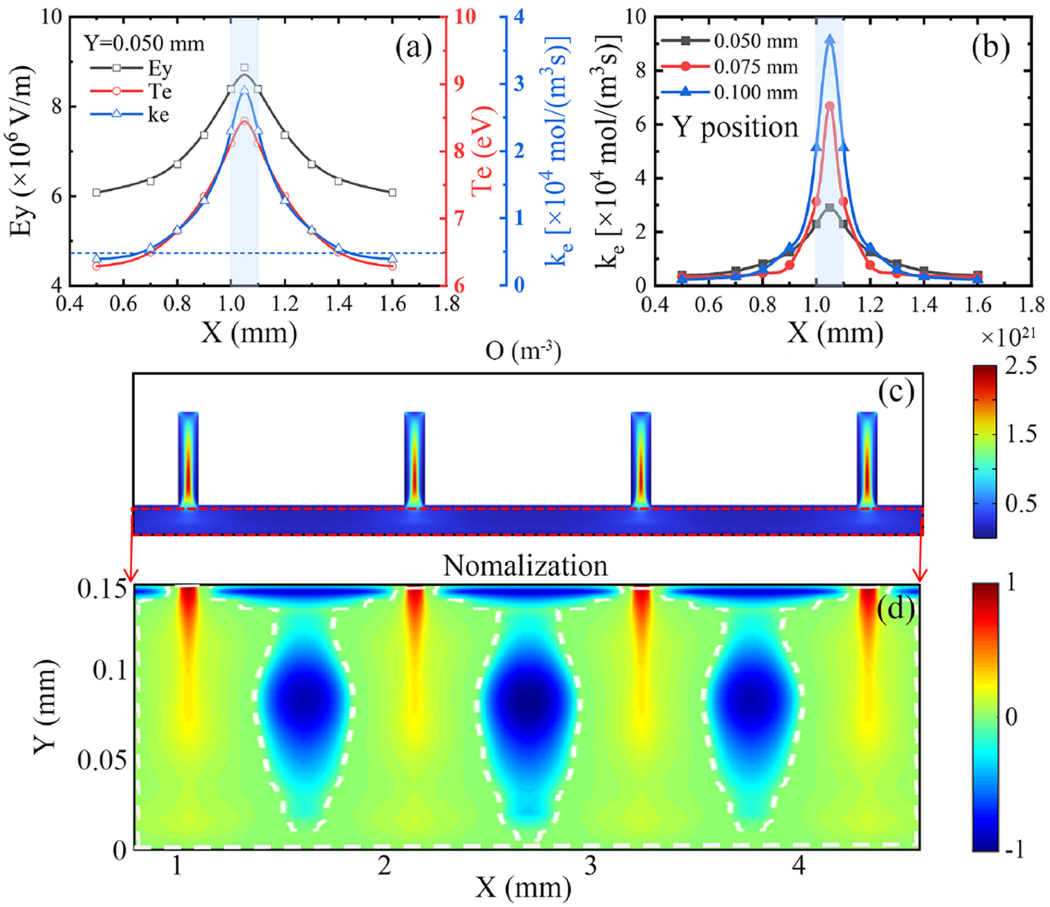

FIG. 9. (a) Peak longitudinal electric field, electron energy, and electron reaction rate along Y = 0.05 mm at different X positions. (b) Electron reaction rate at different Y positions. (c) The spatial distribution of oxygen atoms after the discharge. (d) Normalized difference in O atom distribution after discharge (with–without microstructure) in the bulk discharge region. The study region in (d) corresponds to the red dashed rectangular region indicated in (c).

below the maximum value without microstructures, indicating a localized weakening of the discharge. This weakening is caused by the transverse electric field, which drives electrons away from this region toward the bulk discharge region corresponding to the slit [see Figs. 8(c) and 8(d)]. As a result, the local electron density and ionization capability are reduced. These results clearly demonstrate that the transverse electric field modulates the spatial distribution of electrons and significantly influences the intensity of electron collision reactions in different regions. Consequently, it plays a key regulatory role in discharge behavior.

Figure 9(b) further illustrates the electron reaction rate at different Y positions. As the position approaches the grounded electrode, the peak reaction rate decreases from 9.15×10^4 to 2.90×10^4 mol m^{-3} s^{-1}. This trend indicates a reduction in the number of energetic electrons and a weakening of the discharge-enhancing capability. The smallest enhancement range is observed at Y = 0.075 mm, suggesting that the effect of the slit is spatially limited.

As shown in Fig. 9(c), the peak spatial density of oxygen atoms after the micro-discharge reaches 10^{21} m^{-3}, which is consistent with reports in related literature.[44,49] The oxygen atom density inside the slit is notably high, indicating strong ionization reactions. This trend is consistent with phenomena observed in relevant experiments.[18]

Furthermore, the discharge-promoting range in the bulk discharge region was analyzed, and the results are shown in Fig. 9(d). The figure presents the normalized difference in atomic oxygen density between the microstructured and non-microstructured conditions after the rising edge of the discharge. Positive values (>0) correspond to regions of discharge enhancement, whereas negative values (<0) indicate discharge suppression. The region enclosed by the white dashed line denotes the region where the discharge is significantly promoted. These results indicate that the microstructure enhances the generation of atomic oxygen over a broad region of the bulk discharge zone. The comprehensive analysis shows that the ionization wave enhanced by the slit structure enters the bulk discharge region. Its longitudinal electric field is continuously extended through the corresponding slit and radiates to both sides of the bulk discharge region. This behavior forms a discharge enhancement mechanism dominated by longitudinal electric-field superposition and supported by transverse electron drift. The mechanism increases local electron energy and reaction activity. It also redistributes electrons to key regions,

thereby expanding the effective discharge zone and intensifying the discharge strength.

IV. SUMMARY

In summary, this study demonstrates that sub-millimeter microstructures can effectively modulate atmospheric pulsed discharge. Two-dimensional numerical simulations reveal a multi-region synergistic mechanism. This mechanism is mediated by the coordinated action of longitudinal and transverse electric fields. The longitudinal electric field drives the formation and propagation of the ionization wave. The locally enhanced ionization wave further radiates into the bulk discharge region. There, it superimposes with the external electric field, jointly enhancing the local electric field and electron energy. Meanwhile, the transverse electric field guides electrons toward the ionization wavefront. This process optimizes the spatial charge distribution and helps sustain high plasma reactivity. To optimize the discharge performance, reducing the spacing between the slits allows the oppositely directed transverse electric fields generated by adjacent slits to partially cancel each other, thereby decreasing electron losses in the bulk discharge region corresponding to the dielectric. Meanwhile, the longitudinal electric fields produced by neighboring slits superpose with each other, resulting in a more spatially uniform longitudinal electric-field distribution and, consequently, improved discharge uniformity. This microstructured configuration enhances the discharge performance by regulating electron dynamics and effectively reconstructing the local spatial electric-field distribution. Given that electron dynamic processes share common characteristics across different gas discharge systems, this microstructural strategy is also applicable to other gas discharge conditions. This microstructure-based control method provides a new pathway for efficiently generating reactive oxygen species (including high-concentration ozone). It demonstrates significant advantages in applications such as polymer surface modification, micro–nano patterning based on active species concentration gradients, and localized surface activation.

SUPPLEMENTARY MATERIAL

See the supplementary material for oxygen reaction equations and validation work.

ACKNOWLEDGMENTS

This work was funded by the Natural Science Foundation of China (Nos. 12175036 and 12475259).

AUTHOR DECLARATIONS

Conflict of Interest

The authors have no conflicts to disclose.

Author Contributions

Junlin Fang: Conceptualization (equal); Data curation (equal); Formal analysis (equal); Investigation (equal); Methodology (equal); Software (equal); Supervision (equal); Validation (equal); Visualization (equal); Writing – original draft (equal). **Bingbing Gu:** Conceptualization (equal); Data curation (equal); Formal analysis (equal); Methodology (equal); Software (equal); Validation (equal). **Miao Wang:** Formal analysis (equal); Investigation (equal); Methodology (equal); Software (equal); Validation (equal). **Shaofeng Xu:** Conceptualization (equal); Data curation (equal); Formal analysis (equal); Investigation (equal); Methodology (equal); Resources (equal); Supervision (equal); Validation (equal). **Yongfeng Mei:** Conceptualization (equal); Data curation (equal); Formal analysis (equal); Investigation (equal); Methodology (equal); Resources (equal); Supervision (equal); Validation (equal). **Ying Guo:** Conceptualization (equal); Formal analysis (equal); Funding acquisition (equal); Investigation (equal); Methodology (equal); Project administration (equal); Resources (equal); Software (equal); Supervision (equal); Validation (equal); Visualization (equal); Writing – review & editing (equal). **Jianjun Shi:** Conceptualization (equal); Formal analysis (equal); Funding acquisition (equal); Investigation (equal); Methodology (equal); Project administration (equal); Resources (equal); Supervision (equal); Validation (equal); Visualization (equal); Writing – review & editing (equal).

DATA AVAILABILITY

The data that support the findings of this study are available within the article and its supplementary material.

REFERENCES

[1]T. von Woedtke, M. Laroussi, and M. Gherardi, "Foundations of plasmas for medical applications," Plasma Sources Sci. Technol. **31**(5), 054002 (2022).
[2]S. Wu, Z. Wang, Q. Huang, X. Tan, X. Lu, and K. Ostrikov, "Atmospheric-pressure plasma jets: Effect of gas flow, active species, and snake-like bullet propagation," Phys. Plasmas **20**(2), 023503 (2013).
[3]T. von Woedtke, S. Emmert, H.-R. Metelmann, S. Rupf, and K.-D. Weltmann, "Perspectives on cold atmospheric plasma (CAP) applications in medicine," Phys. Plasmas **27**(7), 070601 (2020).
[4]Y. Akishev, S. Ermolaeva, M. Medvedev, A. Petryakov, K. Hajisharifi, H. Mehdian, and E. Robert, "On spatial-temporal plasma structure behavior inside and outside the discharge zone of a sinusoidal coaxial DBD in argon flow at atmospheric pressure," Phys. Plasmas **32**(9), 093512 (2025).
[5]Y. Akishev, S. Ermolaeva, M. Medvedev, A. Petryakov, K. Hajisharifi, H. Mehdian, and E. Robert, "Coaxial barrier discharge in argon flow excited by pulse groups of periodic voltage: Plasma structures formation in the discharge zone and plasma jet," Phys. Plasmas **32**(7), 073501 (2025).
[6]S. Muradia and M. Nagatsu, "Low-voltage pulsed plasma discharges inside water using a bubble self-generating parallel plate electrode with a porous ceramic," Appl. Phys. Lett. **102**(14), 144105 (2013).
[7]C. Duan, M. Tanaka, M. Kishida, and T. Watanabe, "Treatment of pyridine in industrial liquid waste by atmospheric DC water plasma," J. Hazard. Mater. **430**, 128381 (2022).
[8]G. Y. Park, S. J. Park, M. Y. Choi, I. G. Koo, J. H. Byun, J. W. Hong, J. Y. Sim, G. J. Collins, and J. K. Lee, "Atmospheric-pressure plasma sources for biomedical applications," Plasma Sources Sci. Technol. **21**(4), 043001 (2012).
[9]A. Shashurin, M. Keidar, S. Bronnikov, R. A. Jurjus, and M. A. Stepp, "Living tissue under treatment of cold plasma atmospheric jet," Appl. Phys. Lett. **93**(18), 181501 (2008).
[10]J. Wang, M. Wang, J. Fang, S. Xu, Y. Guo, K. Ding, and J. Shi, "Plasma-activated water: Effects of gas-liquid interface interaction and discharge intensity on activation properties," Phys. Plasmas **32**(3), 033505 (2025).
[11]N. Boysen, T. Hasselmann, S. Karle, D. Rogalla, D. Theirich, M. Winter, T. Riedl, and A. Devi, "An N-heterocyclic carbene based silver precursor for plasma-enhanced spatial atomic layer deposition of silver thin films at atmospheric pressure," Angew. Chem., Int. Ed. **57**(49), 16224–16227 (2018).
[12]J. H. Han, E. Ungur, A. Franquet, K. Opsomer, T. Conard, A. Moussa, S. De Gendt, S. Van Elshocht, and C. Adelmann, "Atomic layer deposition of tantalum oxide and tantalum silicate from $TaCl_5$, $SiCl_4$, and O_3: Growth behaviour and film characteristics," J. Mater. Chem. C **1**(37), 5981 (2013).
[13]Y. K. Sun, G. D. Zhang, L. Hu, R. R. Zhang, R. H. Wei, X. B. Zhu, and Y. P. Sun, "Facile synthesis of vanadium oxide thin films by atomic layer deposition and post-annealing," Appl. Phys. Lett. **126**(5), 051902 (2025).

[14]C. D. C. Pangilinan, W. Kurniawan, and H. Hinode, "Effect of MnOx/TiO_2 oxidation state on ozone concentration in a nonthermal plasma-driven catalysis reactor," Ozone **38**(2), 156–162 (2016).
[15]J. Li, J. Yao, F. He, and J. Ouyang, "Comparison of ozone production in planar DBD of different modes," Plasma Chem. Plasma Process. **44**(2), 891–905 (2024).
[16]C. Liang, Z. Liu, B. Sun, H. Zou, and G. Chu, "Improvement in discharge characteristics and energy yield of ozone generation via configuration optimization of a coaxial dielectric barrier discharge reactor," Chin. J. Chem. Eng. **60**, 61–68 (2023).
[17]S. Jodzis and M. Zieba, "Energy efficiency of an ozone generation process in oxygen. Analysis of a pulsed DBD system," Vacuum **155**, 29–37 (2018).
[18]M. Li, Y. Yan, L. Zhang, Z. Zhou, L. Zheng, B. Zhu, L. Wang, T. Li, X. Tang, and Y. Zhu, "Promoting ozone synthesis from oxygen by a high performance volume-surface hybrid discharge," Appl. Phys. Lett. **114**(11), 114102 (2019).
[19]X. Wang, T. Shao, J. Qin, Y. Li, X. Long, D. Jiang, and J. Ding, "Promotion effect of micro-hole in dielectric on ozone generation of dielectric barrier discharge," Ozone **46**(4), 345–354 (2024).
[20]X. Wang, Q. Huang, S. Ding, W. Liu, J. Mei, Y. Hunag, J. Luo, L. Lei, and F. He, "Micro hollow cathode excited dielectric barrier discharge (DBD) plasma bubble and the application in organic wastewater treatment," Sep. Purif. Technol. **240**, 116659 (2020).
[21]M. Li, Y.-M. Zhu, D.-P. Wu, X.-Z. Zhang, J. Guo, B. Zhu, and K. Jiang, "Enhancement of ozone synthesis via ZnO coating for hybrid discharge in pure oxygen," Plasma Chem. Plasma Process. **41**(6), 1595–1611 (2021).
[22]L. Wei, Q. Deng, and Y. Zhang, "Ozone generation enhanced by silica catalyst in oxygen-fed dielectric barrier discharge," Vacuum **173**, 109145 (2020).
[23]G. V. Naidis and N. Y. Babaeva, "Electric field distributions along helium plasma jets," High Voltage **5**(6), 650–653 (2020).
[24]B. Ghimire, E. J. Szili, and R. D. Short, "A conical assembly of six plasma jets for biomedical applications," Appl. Phys. Lett. **121**(8), 084102 (2022).
[25]J. L. Walsh, J. J. Shi, and M. G. Kong, "Contrasting characteristics of pulsed and sinusoidal cold atmospheric plasma jets," Appl. Phys. Lett. **88**(17), 171501 (2006).
[26]H. Jiang, T. Shao, C. Zhang, Z. Niu, Y. Yu, P. Yan, and Y. Zhou, "Comparison of AC and nanosecond-pulsed DBDs in atmospheric air," IEEE Trans. Plasma Sci. **39**(11), 2076–2077 (2011).
[27]Q. Wang, F. Liu, C. Miao, B. Yan, and Z. Fang, "Investigation on discharge characteristics of a coaxial dielectric barrier discharge reactor driven by AC and ns power sources," Plasma Sci. Technol. **20**(3), 035404 (2018).
[28]C. Miron, M. A. Bratescu, N. Saito, and O. Takai, "Effect of the electrode work function on the water plasma breakdown voltage," Curr. Appl. Phys. **11**(5), S154–S158 (2011).
[29]Y. Hayashi, Wahyudiono, S. Machmudah, N. Takada, H. Kanda, K. Sasaki, and M. Goto, "Decomposition of methyl orange using pulsed discharge plasma at atmospheric pressure: Effect of different electrodes," Jpn. J. Appl. Phys. **53**(1), 010212 (2014).
[30]P. Liu, Y. Song, and Z. Zhang, "A novel dielectric barrier discharge (DBD) reactor with streamer and glow corona discharge for improved ozone generation at atmospheric pressure," Micromachines **12**(11), 1287 (2021).
[31]J. Fang, Y. Zhang, C. Lu, L. Gu, S. Xu, Y. Guo, and J. Shi, "Electron characteristics and dynamics in sub-millimeter pulsed atmospheric dielectric barrier discharge," Chin. Phys. B **33**(1), 015201 (2024).
[32]Y. Zhang, J. Fang, S. Xu, Y. Guo, and J. Shi, "Asymmetrical ignition of radio frequency discharge in atmospheric pressure cascade glow discharges," Plasma Sources Sci. Technol. **32**(3), 035003 (2023).
[33]C. Lu, S. Xu, Y. Mei, G. Huang, Y. Guo, and J. Shi, "Discharge dynamics of ionization wave manipulated by electrical potential amplitudes in atmospheric pressure plasma jet," Appl. Phys. Lett. **126**(24), 244102 (2025).
[34]C. Lu, J. Fang, S. Xu, Y. Guo, and J. Shi, "Manipulating the propagation of ionization wave by pulsed electrical potential in atmospheric plasma jet," Appl. Phys. Lett. **123**(11), 114104 (2023).
[35]X. Han, X. Wei, H. Xu, W. Zhang, Y. Li, Y. Li, and Z. Yang, "Investigation on the parameter distribution of Ar/O_2 inductively coupled plasmas," Vacuum **168**, 108821 (2019).
[36]S. Elaissi, E. M. Moneer, N. A. M. Alsaif, and S. Gouadria, "Double inductively coupled plasma using Ar/O_2 for biomedical implants sterilization and large polymer surfaces decontamination," J. Vac. Sci. Technol., A **43**(5), 054002 (2025).
[37]Y. Yoshida and T. Sakurai, "High-density plasma produced by a holey-plate surface-wave structure cavity," Jpn. J. Appl. Phys. **37**(10), 5746–5750 (1998).
[38]Y. Yoshida, "Disk plasma generation using a holey-plate surface-wave structure on a coaxial waveguide," Rev. Sci. Instrum. **69**(5), 2032–2036 (1998).
[39]F. Medina, F. Mesa, and R. Marques, "Extraordinary transmission through arrays of electrically small holes from a circuit theory perspective," IEEE Trans. Microwave Theory Tech. **56**(12), 3108–3120 (2008).
[40]J. Fang, B. Gu, S. Xu, Y. Mei, Y. Guo, and J. Shi, "Synergistic enhanced oxygen pulsed discharge by surface micro-groove structures at atmospheric pressure," Appl. Phys. Lett. **127**(7), 074101 (2025).
[41]S. Kelly and M. M. Turner, "Atomic oxygen patterning from a biomedical needle-plasma source," J. Appl. Phys. **114**(12), 123301 (2013).
[42]X. Li, P. Zhang, P. Jia, J. Chu, and J. Chen, "Generation of a planar direct-current glow discharge in atmospheric pressure air using rod array electrode," Sci. Rep. **7**(1), 2672 (2017).
[43]S. S. Tabaie, D. Iraji, and R. Amrollahi, "Measurement of electron temperature and density of atmospheric plasma needle," Vacuum **182**, 109761 (2020).
[44]A. Starikovskiy and N. Aleksandrov, "Plasma-assisted ignition and combustion," Prog. Energy Combust. Sci. **39**(1), 61–110 (2013).
[45]M. O. Hassan, A. Nojeh, and K. Takahata, "Effects of electrode shape in micro-electro-discharge patterning of carbon nanotube forests," Precis. Eng. **89**, 46–54 (2024).
[46]G. V. Naidis and N. Yu. Babaeva, "On propagation of positive and negative streamers in air in uniform electric fields," Phys. Lett. A **482**, 129037 (2023).
[47]J. Zhou, Y. Zhang, Z. Luo, Q. Zhang, and L. Wang, "Tip-effect-driven field enhancement and faster mass transport and their advanced applications," Chem. Commun. **61**(52), 9343–9358 (2025).
[48]C. Ding, D. Yuan, Z. Wang, Y. He, S. Kumar, Y. Zhu, and K. Cen, "Ozone production influenced by increasing gas pressure in multichannel dielectric barrier discharge for positive and negative pulse modes," Ozone **40**(3), 228–236 (2018).
[49]L.-S. Wei, B.-F. Peng, M. Li, and Y.-F. Zhang, "A numerical study of species and electric field distributions in pulsed DBD in oxygen for ozone generation," Vacuum **125**, 123–132 (2016).